Mantle flow entrained by the Hindu Kush continental subduction inferred from source-side seismic anisotropy

Cheng-Chien Peng[1], Ban-Yuan Kuo[2], Manuele Faccenda[3], and Ling-Yun Chiao[1]

[1] Institute of Oceanography, National Taiwan University, Taipei, Taiwan
[2] Institute of Earth Sciences, Academia Sinica, Taipei, Taiwan
[3] Dipartimento di Geoscienze, Università di Padova, Padova, Italy

Corresponding author: Ban-Yuan Kuo (byk@earth.sinica.edu.tw)

Hightlights:

• Circular pattern of shear wave splitting was found around the Hindu Kush slab

• Such pattern can be induced by either slab rollback or subduction entrainment

• The subduction entrainment is likely the primary cause

• A-type olivine with strong orthorhombic anisotropy is needed in the entrainment model

Keywords:

Continental subduction, sub-slab mantle, slab breakoff, subduction entrainment, seismic anisotropy, Hindu Kush

Abstract

The intermediate-depth seismicity below the Hindu-Kush orogen is thought to mark the Indian-plate subduction with the bottom half of the slab currently breaking off. Unique features of this continental subduction are the near-vertical slab and the roughly stationary convergence boundary. How this subduction affects the mantle flow patterns remains to be understood. In this study we measured source-side shear wave splitting on the S waves from Hindu Kush intraslab events to sample the surrounding mantle. The observed fast polarization directions exhibit a circular pattern around the slab resembling that predicted for the toroidal flow driven by slab rollback. However, the rollback scenario is not favored because it hardly sustains in dynamic models without a considerable retreat of convergence boundary. We propose that the observed pattern is produced by the sub-vertical shear flow entrained by the steep descent of the slab and the ongoing breakoff. This scenario requires the existence of A-type or AG-type olivine fabrics with strong orthorhombic anisotropy in mid- to lower upper mantle, which is consistent with the global models of azimuthal and radial anisotropy. This interpretation circumvents the debate on the cause of trench-parallel anisotropy in some oceanic subduction zones where slab entrainment and rollback may coexist, and supports the notion that orthorhombic anisotropy of olivine may play an important role in shaping mantle anisotropy.

1. Introduction

1.1 The Hindu Kush-Pamir mountain belt

The collision of the Indian sub-continent with the Eurasian plate created the Himalaya and Tibetan plateau with a well-illuminated underthrusting of the Indian crust and lithosphere (Schulte-Pelkum, 2005; Nábelek, et al., 2009). In the eastern Himalayan syntaxis, the Indian indention produced large-scale lateral extrusion of the Eurasian crust and lithosphere without an obvious trace of deep subduction. Around the western edge of the Indian indenter lies the Hindu Kush (HK) and Pamir mountain belt, where intermediate-depth earthquakes extend to 250 km depth (Fig. 1). This seismic zone has been linked to the subduction of either of the two continental plates, as geological and geophysical evidence has ruled out the involvement of the Tethyan oceanic lithosphere (Burtman and Molnar, 1993; Sippl et al., 2013; Schnieder et al., 2013; Li et al., 2018).

The seismicity-depicted slabs are near-vertical beneath the Hindu Kush (Sippl et al., 2013) and dipping southward beneath the Pamir (Schneider et al., 2013). Whether the seismicity arises from subduction of the Indian or the Eurasian plate has been debated (e.g., Burtman and Molnar, 1993; Pavlis and Das, 2000; Sippl et al., 2013). Up to date, the Pamir's Eurasian origin has become widely accepted (Schnieder et al., 2013) because of the apparent southward dipping. The steep geometry of the HK slab, however, has rendered its provenance less certain. Recent tomographic imaging (Kufner et al., 2016) suggests the association of the HK slab with the Indian plate based on the spatial relationship between the high velocity anomalies and the seismicity. P wave images reveal that the Hindu Kush slab reaches 600 km depth, much deeper than the terminal depth of the seismicity at 250 km. The shape of the velocity anomalies, together with the kinematics of the earthquake sources, suggest that the aseismic part of the slab is in the process of breaking off (Kufner et al., 2017).

Previous studies have suggested a wide range of evolution models for the HK-Pamir double verging system. The Pamir subduction might have commenced at 15-25 Ma (Sobel et al., 2013) with a northward retreating plate boundary over a distance of 300 km, now at the Main Pamir

Thrust (Fig. 1). The Indian subduction in the Hindu Kush has been thought to start either at 8 Ma (Negredo et al., 2007) or slightly predating 11 Ma (Kufner et al., 2016). In contrast to the Pamir, the HK convergence boundary has remained roughly stationary (Replumaz and Tapponnier, 2003). However, the straightening of the slab may be partially caused by the "trench" (hereafter we use trench to represent the convergence plate boundary in the HK region) advancing pushed by the Indian indention, implying that the boundary might have even migrated northward over a short distance (Liao et al., 2017). The continental subduction in general, and the HK-Pamir two-slab system specifically, have attracted modeling efforts mainly on the dynamic evolution of the slab or its impact on the orogen evolution (e.g., Duretz et al., 2012; Duretz and Gerya, 2013; Krystopowicz and Currie, 2013; Liao et al., 2017). How the continental subduction together with the breakoff may shape the mantle dynamics in the region has remained poorly understood.

1.2 Shear wave splitting and sub-slab dynamics

Compared to continental subduction, the mantle response to oceanic subduction has been widely investigated primarily using the observations of seismic anisotropy. Seismic anisotropy is a phenomenon resulting from systematic alignment of intrinsically anisotropic minerals through crystal viscous deformation. One of the most direct forms of anisotropy is shear wave splitting (SWS), which involves separation of an S-wave phase into two quasi phases polarized in planes parallel to the directions of fast and slow velocity of the anisotropic medium. For vertically incident S waves, SWS observations map the anisotropy in planform. SKS is the most commonly utilized phase for SWS observations due to its advantage that the observed anisotropy is known to be associated with the upswing path. The provenance of anisotropy can be further narrowed down to upper mantle according to SKS sensitivity kernels computed for different anisotropic parameters

(Sieminski et al., 2007). In principle, teleseismic direct S phase can be used as long as the path is sufficiently vertical. In the source-side anisotropy approach using direct S wave, receiver-side anisotropy is usually constrained by SKS splitting and removed (e.g., Russo and Mocanu, 2009; Long, 2013). Both SKS and source-side anisotropy studies have helped to delineate the structures of the mantle disturbed by oceanic subduction zones (e.g., Long, 2013).

In sub-slab mantle, slab entrainment and rollback together generate a 3D flow. Observed anisotropy with fast directions perpendicular to subduction zone trenches is often attributed to the slab entrainment or the poloidal component of the 3D flow, whereas trench-parallel splitting is thought to result from the rollback-induced toroidal flow (e.g., Long, 2013; Faccenda and Capitanio, 2012; 2013). This interpretation in which each flow component is responsible for one particular anisotropy pattern has been appealing because it involves only one type of deformation pattern for olivine (the most abundant mineral in the upper mantle), i.e., A-type lattice preferred orientation (LPO), which is characterized by the easy slip system [100](010), in which olivine a-axis [100] is parallel to the shear direction and b-axis perpendicular to, or the b-plane (010) parallel to, the shear plane (e.g., Karato, 2008). However, the association of trench-parallel anisotropy solely with the toroidal flow has recently been challenged. Song and Kawakatsu (2012; 2013) argued that some of the trench-parallel anisotropy observations can be explained instead by subduction entrainment of the asthenosphere if the slab is sufficiently steep. Walpole et al. (2017) proposed a similar model with the term of "tilted transverse isotropy (TTI)" to explain the trench-parallel pattern in the sub-slab mantle. Lynner and Long (2014) asserted that the trench-parallel splitting tends to occur in old subduction zones where toroidal flow dominates while the trench-normal splitting characterizing most of the young subduction zones are driven by slab entrainment.

Different LPOs of olivine, such as C-type with [001](100) and E-type with [100](001) (e.g., Karato, 2008), may also play important roles in shaping anisotropy patterns in the sub-slab mantle (Lynner et al., 2017). The sub-vertical slab of HK could serve as a continental test site on the controversies inherited from oceanic subduction zones.

In this study we conduct source-side shear wave splitting analysis for the HK region, which allows mapping of the deformation structure surrounding the subduction zone (e.g., Russo and Silver, 1994; Long, 2013). An earlier attempt of this kind in this region (Schoenecker et al., 1997) employed limited data and provided preliminary interpretations. In a recent study using SKS across the HK-Pamir orogenic belt (Kufner et al., 2018), the splitting exhibits mainly ENE trending fast polarization directions suggesting an indention-escape process in the lithosphere and asthenosphere. Here we analyze a large set of source-side SWS data in the HK subduction zone to constrain the dynamics in mid- to lower upper mantle surrounding the HK slab that is independent of the lithospheric processes related to the development of the orogen.

2. Data and method

Our data set consists of 58 new measurements of source-side anisotropy for 32 events in the HK subduction zone in a depth range of 70-240 km with sources primarily concentrated at 100 and 200 km depths. We assume that the down-going S waves from the HK subduction zone sample the anisotropy mainly in the depth range from the source to 410 km, because in the transition zone single crystal wadsleyite has much lower anisotropy than olivine (Zhang et al., 2018). The event magnitudes range from Mw 5.5 to 7.3, and epicentral distances from 41 to 74^{o} (Details of events and stations used can be found in Supplementary Table S1). The most common practice in the receiver-side correction is to remove the anisotropy constrained by the SKS splitting. It is thus critical that the SKS splitting data represent properly the overall upper mantle properties beneath the station, which can be azimuthally dependent and even varying with depth. In their studies, Lynner and Long (2014) and Mohiuddin et al. (2015) have selected stations that show SKS splitting reasonably uniform under sufficient azimuthal coverage such that the upper mantle anisotropy beneath the station can be well characterized by one set of splitting parameters, including the null solutions. This ensures that the SKS-based receiver-side correction is unbiased for direct S waves from all azimuths. In this study, we used 11 stations, which are all noted in these two previous studies as having either null or simple form of azimuthal anisotropy that can provide proper receiver-side correction (see Table S1).

Another issue about receiver-side correction is the possible bias by neglecting the effect of radial anisotropy in the upper mantle beneath the station. As the incidence angle increases, direct S is more sensitive to the radial anisotropy than SKS. Our past experience indicates that the sensitivity is a complex function of backazimuth and polarization direction, and that, even though when individual measurements differ substantially with and without radial anisotropy in the receiver-side correction, the overall pattern of SWS largely remains. This is because, in the case we examined, the multiple sources and paths used render random scatters from the original splitting that together do not shift the pattern in any systematic way. Moreover, radial anisotropy models themselves carry uncertainties. In this study, we do not consider the effect of radial anisotropy in the receiver-side correction.

The standard routine of receiver-side correction involves rotating the NS and EW components of S wave to the fast and slow directions at the station determined from SKS anisotropy measurements, closing the time shift (δt) between the two phases, and rotating the waveforms back to the NS and EW directions. After the correction is finished, we apply our SWS measurement routine (e.g., Kuo et al., 2012; Kuo et al., 2018; details to be discussed below and in Supplementary) to obtain the splitting parameters (ϕ_r,δt), where ϕ_r is the fast direction on the receiver side. One unique step in the source-side splitting approach is the geometrical correction that translates ϕ_r in the station frame to ϕ in the source frame using $\phi = \alpha + \beta - \phi_r$ (Nowacki et al., 2015), where α is the azimuth of the S wave at the source and β is the backazimuth at the receiver. Examples of measurement are shown in Fig. 2. The quality control criteria follow that practiced by Kuo et al. (2018) for SKS, which includes a comparison between results from rotation-correlation and minimum Eigenvalue methods (details in Supplementary). In this study, the splitting parameters from the minimum eigenvalue method are reported. The last step of the quality control in Kuo et al. (2018) is to require small deviation of the recovered particle motion from the SKS great-circle path. For source-side anisotropy, this step is replaced by comparing the final particle motion against that calculated from centroid-moment tensor (CMT) solution of the source (e.g., Ekström et al., 2012). We abandoned those with the difference greater than 15^{o} (Fig. 2; Fig. S1 in Supplementary). We also determined the null solutions following the approach of Wüstefeld and Bokelmann (2007) (Supplementary). The comparison with the nulls are explained below.

3. Pattern of source-side splitting

Fig. 3 shows the pattern of shear wave splitting plotted at locations 200 km down dip from respective earthquakes along the S wave paths traced in iasp91 global velocity model (Kennett and Engdahl, 1991) using the TauP program (Crotwell et al., 1999). The eight measurements from Schoenecker et al. (1997) were included in this figure. Measurement results are summarized in Table S2. The prominent features are the consistent alignment of fast polarization direction ϕ in parallel with the general trend of the trench on the Indian side in group A and a clustering of ϕ oblique to the trench northwest of the HK on the Asian side in group B. Group C consists of a small number of measurements with paths crossing the back of the Pamir subduction zone (northern side), yielding scattered results although with an apparent EEW majority. Group D samples the east of HK and the south of the Pamir. From D1 to D2, ϕ exhibits a rotation from normal to oblique with respect to the strike of the Pamir slab.

The patterns of ϕ in groups A, B, D1 and D2 are in general compatible with that of the null solutions, which is an independent constraint on the reliability of the measurements (Fig. S2). Furthermore, group A consists of three stations of null anisotropy straddling from oceanic hotspot (RER) to the margin of the craton in southern Africa (LSZ), yet the observed splitting directions are highly consistent as shown in the rose diagram in Fig. 3, implying that the observed splitting originates from near-source structures. In other groups, stations do not spread in space like in group A so that this argument does not apply. Nonetheless, the stringent quality control, the general agreement with the nulls, the selection of stations from Lynner and Long (2014) and Mohiuddin et al. (2015), and the implication from group A together lend us confidence that our measurements are reliable and their source-side origin is valid.

Three-dimensional visualization shows that the S waves sample the upper mantle surrounding the steep HK seismic zone (Fig. 4). The delay times are 1 – 3 s (Fig. S3), which would need an S wave traveling for 100-400 km long in a 3-4% anisotropy domain. To estimate how slab anisotropy may contribute to the final results, we calculate the path length of the S wave traveling inside the slab compared with the total length from the source to the 410 km depth. We use 1, 1.5, and 2% velocity perturbations in Kufner et al.'s (2016) tomographic model to define the outer boundary of the slab. As this threshold increases, the path length through the slab decreases. Low threshold pushes the boundary towards the surrounding mantle where fossil anisotropy may not sustain. Overall, there is no correlation of splitting parameters with the slab path length. For 1.5 and 2%, the S waves in groups A and B rarely travel through any slabs, while group D still has high percentage of paths in the Pamir slab (Fig. S4). There is no direct evidence for the presence of frozen-in anisotropy in the HK or Pamir subduction zones. If it is any hint, Kufner et al.'s (2018) local-event and teleseismic SKS anisotropy measurements show ESE- and ENE-oriented ϕ for crust and lithosphere, respectively, north of the plate boundary. If these fabrics remain frozen-in after the Pamir subduction, then this hypothetical fossil ϕ are at odds with the observations of D group. Details of possible slab effect is discussed in Supplementary (Fig. S4). We assume that groups A, B, and D primarily detect the deformation in the mid- to lower upper mantle surrounding the HK subduction zone.

Groups A and D exhibit little depth dependence of splitting parameters, while in B, ϕ rotates roughly from NS to NE-SW and δt slightly decreases with event depth (Fig. S1). While groups A and D agree well with the null solution, in B, one peak of ϕ is consistent with the majority of the null solutions and the other peak deviates from the nulls by about 30 ^{o}. Group B probably samples more complex mantle structures than A and D. Nevertheless, the overall orientations of ϕ in the NE-SW quadrants is believed to be a robust feature. In comparison, group C is composed of much fewer data than other groups, and we defer the interpretation of the pattern presented by group C until more data are available.

4. Interpretations

4.1 Slab rollback

Different mechanisms may be involved in producing the observed anisotropy pattern. First, groups A and B together are consistent with that expected for A-type LPO of olivine aligned by the toroidal flow from sub-slab to supraslab mantle (Fig. 5a). This would require a southward rollback of the HK slab probably throughout its relatively short subduction history (scenario 1). The model of Faccenda and Capitanio (2012, 2013) predicts that olivine LPO develops in two domains in sub-slab mantle giving different anisotropy: trench-normal right beneath the slab in the entrained mantle, and trench-parallel at greater depth where rollback imposes toroidal flow. The strength of the trench-parallel anisotropy within the latter domain increases progressively toward the slab lateral margins where the divergence of the toroidal flow (and deformation) is larger. Their models therefore predict strong trench-parallel SKS splitting in that domain as observed in many studies (e.g., Baccheschi et al., 2007; Foley and Long, 2011; Lynner and Long, 2013). The source-side anisotropy in this study may result from the toroidal flow in the deeper part of the sub-slab mantle.

Group D covers the region where the two slabs are close to each other, with the wave paths grazing the high velocity core of the lower part of the westernmost Pamir slab (Fig. 4). The apparent rotation in ϕ from D2 to D1 may be related to the same toroidal flow associated with the HK slab that turns counter-clockwise around the eastern edge. On the other hand, the possible northward rollback of the Pamir slab may induce its own toroidal flow that wraps both slab edges. Once turning to the Parmir wedge side (south), both toroidal branches may join the corner flow there to form trench-normal anisotropy (Faccenda and Capitanio, 2012, 2013). Although this is consistent with D1, it should occur inside the mantle wedge, not much beneath it. The rollback of the Pamir slab may also drive material around the slab tip, but this poloidal type of flow seems difficult to provide large scale, consistent deformation fabrics over depths (e.g. MacDougall et al., 2017) detectable by SWS.

4.2 Subduction entrainment

Another possible mechanism to cause the observed anisotropy pattern is the alignment of A-type olivine with strong orthorhombic anisotropy by vertical flow entrained by the subduction (Scenario 2) (Fig. 5b). Strong orthorhombic anisotropy for both P and S waves is produced by combining azimuthal anisotropy (*Aa*) with a significant, positive radial anisotropy (*Ra*) $\xi > 1$, where $\xi = ({}^{V_{SH}}/_{V_{SV}})^2$. In oceanic regions, global models often shows *Ra* larger than or comparable to *Aa* (Kustowski et al., 2008; Auer et al., 2014). $\xi > 1$ is equivalent to the transverse isotropy with a vertical slow symmetry axis and a horizontal, fast polarization plane (010) (perpendicular to olivine b-axis). Along with subduction, the slow symmetry axis is progressively tilted, and becomes sub-horizontal in steep subduction zones with the fast polarization plane (010) sub-vertical and slab-parallel (Fig. 5) (e.g., Walpole et al., 2017). This would explain group A and potentially group B and D if the vertical flow surrounds the slab. This mechanism was initially proposed by Song and Kawakatsu (2012; 2013) to explain the observed trench-parallel ϕ in oceanic subduction zones with large dip angles. They demonstrated that, for A-type orthorhombic anisotropy of olivine, when the slab progressively steepens, ϕ for a sub-vertically propagating S wave switches from trench-normal to trench-parallel. The near-vertical slab in the HK stands as a vertical end-member of the models tested by Song and Kawakatsu (2012).

The orthorhombic anisotropy compatible with scenario 2 can be realized by the relationship between the three distinct shear moduli in three respective crystal planes as C55 > C66 > C44, where C44 is associated with the (100) plane, C55 with the (010) plane, and C66 with the (001) plane. The above terminology is based on the mineralogy coordinates in which index 1 corresponds to a-axis, index 2 to b-axis, and index 3 to c-axis (Table 1, bottom half). If the LPO is determined in the deformation experiment, usually 1 refers to the lineation or shear direction, 3 refers to the foliation or the shear plane, and 2 refers to that in the shear plane perpendicular to 1. (Table 1, upper half). Fig. 6 illustrates the vertical flow scenario in terms of these 3 shear moduli in mineralogy coordinates (see Fig. S5 for crystal configurations in deformation coordinates). The orthorhombic anisotropy used by Song and Kawakatsu (2012) (SK12) has 2% *Aa* and 3% *Ra* for shear waves (Table 1). In contrast, for single crystal olivine (Zhang et al., 2018) (Z18) *Ra* is relatively reduced compared to *Aa* if deformed as A-type in horizontal flow, because the difference between the horizontally aligned C55 and the average of C66 and C44 is smaller than the difference between C66 and C44 (Fig. 6). We conducted a synthetic waveform experiment (details in Supplementary) to evaluate how different fabrics listed in Table 1 contribute to scenario 2. Because single crystal olivine anisotropy is the building block of mantle anisotropy, Z18 is also tested. The setting of the model is to mimic A-type deformation in an NS-oriented horizontal flow and an EW-striking vertical flow. These two settings can be viewed together as the flow before and after a vertical subduction along a trench striking at an azimuth of 90^{o}. Recently, Lynner and Long (2014) and Lynner et al. (2017) proposed that E- and C-type olivine LPO better explain the pattern of anisotropy in sub-slab mantle than A-type in a suit of subduction zones. We also include E- and C-type olivine in our examination. Their corresponding crystal configurations in deformation coordinates can be found in Fig. S5.

For both horizontal and vertical flow cases, we generate synthetic waveforms with incidence angles *j* of 5^{o} and 30^{o} (roughly the case of this study), and for S wave propagating azimuths from 90 to 270^{o} (see Supplementary). At each azimuth, two polarization angles of S wave were tested: 0 (SV) and 35^{o} from the propagation direction. We measure SWS on the synthetic waveforms as for the real data. No noise is added to the synthetics, but the same quality control as for the real data is applied. In Figs. 7 and 8, only the results for azimuth of 200^{o}, i.e., the azimuth for most of the rays in group A, is displayed. A-, E- and C-type olivine is the focus of this section, and the effects of B-type fabrics will be discussed later.

Fig. 7 shows that for *j* of 5^{o}, A-type SK12 and Z18, C-type J06C, and E-type J06E (see Table 1 for model names) all produce trench-normal ϕ for horizontal flow as expected. For vertical flow, ϕ parallel the trench (or slab) for SK12, but could be off for some non-SV polarizations for Z18. Splitting is minimal for Z18, because C55 (71.74) is almost equal to C66 (71.16) (Fig. 6) and *Aa* > *Ra*, as explained above. C- and E-type LPOs yield splitting perpendicular and oblique to the trench, respectively. For $j = 30^{o}$, scatter increases. For horizontal flow, ϕ still cluster roughly in the trench-normal regime ($<40^{o}$). In the case of vertical flow, SK12 stably produce splitting in parallel to the trench. An incidence angle of 30^o yields enhanced splitting for Z18, but ϕ is no longer trench-parallel. Splitting for both J06C and J06E is more of trench-normal than of trench-parallel, and thus both C- and E-type fabrics fail to explain our observations. This could be understood intuitively from the fact that C55 (trench-normal) is larger than C66 (trench-parallel) for both C- and E-type olivine in vertical flow environment (Fig. S5). These synthetic experiments demonstrate that the vertical flow model is valid if the dominant mantle mineral olivine deforms as A-type and has orthorhombic anisotropy with a strong radial component that makes C55 > C66 > C44 (in mineralogy frame). This configuration is compatible with the AG-type olivine fabrics documented by Mainprice (2007).

5. Preferred mechanism

We have simplified the mechanisms behind the observed anisotropy pattern around the HK to two scenarios. While a full understanding of the dynamics of the double-verging HK-Pamir system relies on a detailed simulation yet to be available, critical issues pertaining to each scenario can be assessed to help discriminate which one is more favored than the other.

We first examine whether each scenario is realistic in providing sufficient anisotropy. For the vertical flow scenario, assuming a 150 km wide deformation domain from the vertical slab laterally into the ambient mantle (corresponding to an S traveling distance of roughly 300 km), it takes a vertical distance of 150 km, or 4.3 My with a 35 km/My descending rate, to assemble a finite strain of one (γ = 1), a deformation sufficient for strong alignment. Strain accumulation may have started before subduction, but even though it starts at 100 km depth, γ of 2 can be achieved at 400 km depth. The additional stretching of the lower half of the slab (Kufner et al., 2018) since the breakoff inception accelerates the deformation accumulation. In contrast, trench-parallel anisotropy is aligned by pure shear that results from stretching of the minerals in parallel with the trench when they are pushed away by the retreating slab; it is not straightforward to parameterize the strength of the pure shear. Nonetheless, we note that the slab in HK is short in length, i.e., at 380 km depth before breakoff (Kufner et al., 2016) and only 100 km in half width. As a reference, strong trench-parallel anisotropy is accumulated in subduction models with slabs 300-1000 km in half width continuously extending to and resting on the bottom of the transition zone (Faccenda and Capitanio, 2012; 2013). A robust "core" of toroidal flow as witnessed in the numerical models may not easily be formed due to HK's small dimension, and a weak alignment may be overwhelmed by the later, breakoff-driven accelerated shear flow. The rollback scenario seems to be difficult in producing sufficient amount of anisotropy.

Another challenge for the rollback scenario comes from the constraint that the convergence boundary of the HK is nearly motionless. Recent dynamic models (e.g., Duretz and Gerya, 2013; Krystopowicz and Currie, 2013) show that continental subduction occurs in different styles depending on the rheology structure of crust and mantle, often characterized by lithospheric delamination and slab breakoff. In the case of lower crust subduction, either the slab is short-lived due to frequent, complete breakoff or the delamination of mantle lithosphere rapidly retreats to maintain its entirety. The prominent model feature of "trench retreat" is in contradiction with the non-retreating of the plate boundary along the HK (Replumaz and Tapponnier, 2003; Liao et al., 2017). A case model in Krystopowicz and Currie (2013) that might mimic the HK with a stationary trench and a steep slab before complete breakoff is made of increased strength of lower crust and mantle lithosphere so that the delaminated lithosphere does not retreat and detach easily. In all the cases tested in Duretz and Gerya (2013) and Krystopowicz and Currie (2013), rollback with a fixed hinge at the surface is hardly achievable. In the conceptual rollback orogeny model proposed by Kissling and Schlunegger (2017), trench retreat is a central feature. In the oceanic counterpart, Faccenda and Capitanio (2012) shows that, without hundreds of km of trench retreat, trench-parallel delay times are likely negligible.

A point concerning the vertical entrainment scenario is whether the shear flow is disrupted by the breakoff. If the lower slablet is completely detached, the flow around it can be complicated and systematic anisotropy would be difficult to build. The breakoff models tested in Lin and Kuo (2016) for the Taiwan orogen show that the descending of the slab fragment severely destroys the toroidal flow in the vicinity originating from the adjacent slabs. In Confal et al.' (2018) simulation of eastern Mediterranean subduction, complete slab breakoff induces flow across the slab window that significantly influences the pattern of anisotropy. However, tomography on semi-global (Koulakov, 2011; Van der Voo et al., 1999) and regional (Kufner et al., 2016) scales all portrays the HK slab as a vertical structure continuing to the lower transition zone, which is preferable in harnessing large-scale, vertical shear and align the olivine consistently in the surrounding mantle.

The analyses described above strongly favor vertical entrainment, as opposed to rollback, as the primary mechanism for the observed circular pattern of anisotropy around the HK. If the stationary trench does not permit much changes in subduction trajectory, the near-vertical subduction or delamination entails no toroidal flow. This thereby avoids the debate centered at some oceanic subduction zones where toroidal flow may dominate. Our observations thus demonstrate that slab entrainment is a viable mechanism for trench-parallel anisotropy. The vertical slab in the HK can be regarded as the end-member case of the steep subduction scenario where orthorhombic anisotropy of olivine contributes to the trench-parallel anisotropy.

6. Discussion

6.1 The role of B-type olivine

Since positive radial anisotropy ($\xi > 1$) together with $Ra > Aa$ (observed in horizontal flow regions) are critical factors to the vertical flow scenario, questions may arise as to whether the radial anisotropy commonly observed in asthenosphere beneath oceanic plates (e.g., Kustowski et al., 2008; Auer et al., 2014) persists along subduction zones to deep upper mantle. It has been proposed that radial anisotropy may result from petrological fabrics, such as elongated melt pockets, that would not be entrained with subduction to depth (e.g., Kawakatsu and Utada, 2017). Recent global anisotropy model, however, shows primarily negative radial anisotropy ($\xi < 1$) in the lower upper mantle and transition zone around subduction zones (Ferreira et al., 2019), which can be readily explained as caused by the rotation of the same deformation fabrics from horizontal to vertical during subduction.

Despite the global model of Ferreira et al. (2019) suggests a form of radial anisotropy compatible with our deep entrainment interpretation, it is always desirable to examine other mechanisms that could explain the observations too. One type of olivine fabric may enhance the trench-parallel anisotropy without external mechanisms to maintain large radial anisotropy. Jung (2009) reported that A-type olivine fabric transforms to B-type with [001](010) (the same as A-type except c-axis aligns with the shear direction) by increasing pressure to 3 GPa or 100 km depth. Ohuchi and Irifune (2014) demonstrated more complex transformations of A-type dry olivine at about 220 km to either a mix of B- and C-type at high temperatures similar to oceanic mantle conditions or a B-type alike fabric at temperatures akin to continental environment. Moreover, strong B-type LPO is found in rock samples exhumed from pressure conditions greater than 4 GPa (Lee and Jung, 2015).

We tested the effect of B-type fabrics in the same way as for A-, C- and E-types. Fig. 8 shows that Z18B (Z18, but assuming B-type) and LJ15 (Lee and Jung, 2015) provide strong trench-parallel splitting especially for vertical flow. Both O11 (Ohuchi et al., 2011) and J06B (Jung et al. 2006) are computed from weakly aligned samples and thus produce weak and polarization-dependent anisotropy, but some of them may be marginally detectable. An investigation of Z18 reveals how the vertical flow scenario benefits from B-type fabric: For A-type, the trench-parallel and trench-normal directions are dominated by C55 and C66, respectively, which are almost equal in magnitude in most mineral physics reports (e.g., Zhang et al., 2018); for B-type, the moduli in play are C55 and C44 (see Fig. 6) with C44 (trench-normal) being the smallest shear modulus of single crystal olivine (Table 1). While some of the early experiments of pressure-induced fabric transformation was challenged (e.g., Karato, 2008) and B-type olivine predicts anisotropy at odds with seismology observations in most of oceanic asthenosphere, the HK subduction with an accelerated descent during breakoff may facilitate high shear stress in a dry environment where B-type alike transformation may occur in deeper upper mantle. B-type fabric is characterized by $\xi > 1$ in both horizontal and vertical flow, which may increase the heterogeneity of radial anisotropy portrayed in global models like Ferreira et al. (2019).

6.2 Orogenic processes vs. mantle dynamics

The SKS splitting measurements with nearly consistent ENE trending ϕ by Kufner et al. (2018) (Fig. S6) covers mainly the north of the HK-Pamir convergence boundary and barely overlap groups A, B, and D. They proposed a collision-induced escape process in the mantle that produce the anisotropy in parallel with the general trend of the convergence boundary in the HK-Pamir mountain belt. Schoenecker et al. (1997) suggested that the strain field in the upper mantle is induced by collision and indention of the continental plates. These interpretations are in accordance with the conception of coherent deformation over the depth of large mountain belts (Silver, 1996). In contrast, group A, on the Indian side, is sub-parallel to the trend of the convergence boundary in the HK segment alone, and is attributed to subduction processes below the lithosphere. Our source-side anisotropy shows little direct correlation with the geometry of the HK-Pamir convergence boundary (Fig. 2), nor with the major tectonic structures in the region. For instance, groups A and D strike at high angles with the Chaman fault and the Shyok suture zone, respectively (see Fig. 1).

Evidence has mounted in support of a deep origin for the observed anisotropy along mountain belts. In western Alps, while the SKS pattern apparently tracks the Alps curvature, Barruol et al. (2011) proposed that the source of anisotropy resides in the asthenosphere around the Eurasian continental slab. Kuo et al. (2018) demonstrated quantitatively that ϕ's of SKS in parallel with the structures of the Taiwan orogen are better explained by the interaction between the double verging Ryukyu-Manila subduction zones underlying the broad collision zone. We argue that, whereas collision directly imposes deformation in the lithosphere and builds the mountain, subduction-related dynamics dominates the strain field across the depth of the upper mantle that may lead to patterns of anisotropy coincidently correlated with the trend of the mountain structure or convergence boundary.

7. Conclusions

We measured source-side shear wave splitting for the Hindu Kush region to isolate the mid- to lower upper mantle from the collision processes that built the orogen. The results reflect the dynamics in the mantle dictated by the subduction of the Indian lithosphere. We observed a circular pattern of fast polarization direction surrounding the HK slab, which is similar to that found in many oceanic subduction zones where slab rollback is suggested to drive the toroidal flow and the trench-parallel anisotropy. However, because continental slab rollback is difficult to maintain with a fixed convergence boundary as in the case of Hindu Kush, we interpret the anisotropy pattern as resulting from sub-vertical shear flow in the ambient mantle driven by the steep and probably accelerated descent in the detaching segment of the continental lithosphere beneath the Hindu Kush. This scenario necessitates A-type or AG-type olivine characterized by stronger radial than azimuthal component. Whereas this is our main conclusion, in the case that the orthorhombic anisotropy diminishes with depth we speculate that B-type olivine in dry, deep upper mantle, as has been documented in both laboratory and natural rocks, may potentially contribute to the pronounced trench-parallel anisotropy in this region.

Acknowledgment. We thank three anonymous reviewers for their constructive comments. The research was supported by the Ministry of Science and Technology of Taiwan, Republic of China, under grant MOST 107-2116-M-001-020-MY3.

References

Auer, L., Boschi, L., Becker, T. W., Nissen-Meyer, T., & Giardini, D. (2014). Savani: A variable resolution whole-mantle model of anisotropic shear velocity variations based on multiple data sets. Journal of Geophysical Research: Solid Earth, 119(4), 3006–3034.doi:10.1002/2013jb010773

Baccheschi, P., Margheriti, L., Steckler, M.S., 2007. Sesmic anisotropy reveals focused mantle flow around the Calabrian slab (Southern Italy). Geophys. Res. Lett. 34, L05302. https://doi.org/10.1029/2006GL028899

Barruol, G., Bonnin, M., Pedersen, H., Bokelmann, G. H. R., Tiberi, C., 2011. Belt-parallel mantle flow beneath a halted continental collision: The Western Alps. Earth Planet. Sci. Lett. 302, 429–438. https://doi.org/10.1016/j.epsl.2010.12.040

Burtman, V.S., Molnar, P., 1993. Geological and geophysical evidence for deep subduction of continental crust beneath the Pamir. Spec. Pap., Geol. Soc. Am. 281, 1–76. https://doi.org/10.1130/SPE281-p1

Confal, J.M., Faccenda, M., Eken, T., Taymaz, T., 2018. Numerical simulation of 3-D mantle flow evolution in subduction zone environments in relation to seismic anisotropy beneath the eastern Mediterranean region. Earth Planet. Sci. Lett. 497, 50-61. https://doi.org/10.1016/j.epsl.2018.06.005

Crotwell, H.P., Owens, T.J., Ritsema, J., 1999. The TauP Toolkit: Flexible seismic travel-time and ray-path utilities. Seismol. Res. Lett. 70, 154–160. doi:10.1785/gssrl.70.2.154.

Duretz, T., Schmalholz, S.M., Gerya, T.V., 2012. Dynamics of slab detachment. Geochem. Geophys. Geosyst 13(3), Q03020. http://dx.doi.org/10.1029/2011GC004024

Duretz, T., Gerya, T.V., 2013. Slab detachment during continental collision: Influence of crustal rheology and interaction with lithospheric delamination. Tectonophysics 602, 124–140. https://doi.org/10.1016/j.tecto.2012.12.024

Ekström, G., Nettles, M., Dziewonski, A. M., 2012. The global CMT project 2004-2010: Centroid-moment tensors for 13,017 earthquakes. Phys. Earth Planet. Inter. 200-201, 1-9. doi:10.1016/j.pepi.2012.04.002

Faccenda, M., Capitanio, F.A., 2012. Development of mantle seismic anisotropy during subduction-induced 3-D flow. Geophys. Res. Lett. 39, 11. doi:10.1029/2012GL051988

Faccenda, M., Capitanio, F.A., 2013. Seismic anisotropy around subduction zones: insights from three-dimensional modeling of upper mantle deformation and SKS splitting calculations. Geochem. Geophys. Geosyst. 14. http://dx.doi.org/10.1029/2012GC004451

Foley, B.J., Long, M.D., 2011. Upper and mid-mantle anisotropy beneath the Tonga slab. Geophys. Res. Lett., 38, L02303. doi:10.1029/2010GL046021

Ferreira, A.M.G., Faccenda, M., Sturgeon, W., Chang, S.-J., Schardong, L. 2019. Ubiquitous lower-mantle anisotropy beneath subduction zones. Nat. Geosci. 12, 301-306. https://doi.org/10.1038/s41561-019-0325-7

Jung, H., Katayama, I., Jiang, Z., Hiraga, T., and Karato, S., 2006. Effect of water and stress on the lattice-preferred orientation of olivine. Tectonophysics, 421, 1-22. doi:10.1016/j.tecto.2006.02.011.

Jung, H., Mo, W., Green, H.E., 2009. Upper mantle seismic anisotropy resulting from pressure-induced slip transition in olivine. Nat. Geosci. 2, 73–77. https://doi.org/10.1038/ngeo389

Karato, S.-I., Jung, H., Katayama, I., Skemer, P., 2008. Geodynamic significance of seismic anisotropy of the upper mantle: New insights from laboratory studies. Annu. Rev. Earth Planet. Sci. 36, 59–95. doi:10.1146/annurev.earth.36.031207.124120

Kawakatsu, H., Utada, H. 2017. Seismic and electrical signatures of the lithosphere-asthenosphere system of the normal oceanic mantle. Annu. Rev. Earth Planet. Sci. 45, 139-67. https://doi.org/10.1146/annurev-earth-063016-020319

Kennett, B.L.N., Engdahl, E.R., 1991. Traveltimes for global earthquake location and phase identification. Geophys. J. Int. 105, 429–465. doi:10.1111/j.1365-246X.1991.tb06724.x.

Kissling, E., Schlunegger, F., 2018. Rollback Orogeny Model for the Evolution of the Swiss Alps. Tectonics 37, 1097-1115.https://doi.org/10.1002/2017TC004762

Koulakov, I., 2011. High-frequency P and S velocity anomalies in the upper mantle beneath Asia from inversion of worldwide traveltime data. J. Geophys. Res. 116(B4), 1–22. doi:10.1029/2010JB007938

Krystopowicz, N. J., Currie, C.A., 2013. Crustal eclogitization and lithosphere delamination in orogens. Earth Planet. Sci. Lett. 361, 195-207. https://doi.org/10.1016/j.epsl.2012.09.056

Kufner, S.-K., Schurr, B., Sippl, C., Yuan, X., Ratschbacher, L., Mohammad Akbar, A., et al., 2016. Deep India meets deep Asia: Lithospheric indentation, delamination and break-off under Pamir and Hindu Kush (Central Asia). Earth Planet. Sci. Lett. 435, 171–184. https://doi.org/10.1016/j.epsl.2015.11.046

Kufner, S.-K., Schurr, B., Haberland, C., Zhang, Y., Saul, J., Ischuk, A., & Oimahmadov, I., 2017. Zooming into the Hindu Kush slab break-off: A rare glimpse on the terminal stage of subduction. Earth Planet. Sci. Lett. 461, 127–140. https://doi.org/10.1016/j.epsl.2016.12.043

Kufner, S.-K., Eken, T., Tilmann, F., Schurr, B., Yuan, X., Mechie, J., et al., 2018. Seismic anisotropy beneath the Pamir and the Hindu Kush: Evidence for contributions from crust, mantle lithosphere, and asthenosphere. J. Geophys. Res., Solid Earth 123. https://doi.org/10.1029/2018JB015926

Kuo, B.-Y., Wang, C.-C., Lin, S.-C., Lin, C.-R., Chen, P.-C., Jang, J.-P., Chang, H.-K., 2012, Shear-wave splitting at the edge of the Ryukyu subduction zone, Earth Planet. Sci. Lett., 355-356, 262-270, doi:10.1016/j.epsl.2012.08.005.

Kuo, B.-Y., Lin, S.-C., Lin, Y.-W., 2018. SKS splitting and the scale of vertical coherence of the Taiwan mountain belt. J. Geophys. Res., Solid Earth 123, 1366–1380. https://doi.org/10.1002/2017JB014803

Kustowski, B., Ekstrom, G., Dziewonski, A.M., 2008. Anisotropic shear-wave velocity structure of the Earth's mantle: a global model. J. Geophys. Res. 113, (B06306). doi:10.1029/2007JB005169.

Lee, J., Jung, H., 2015. Lattice-preferred orientation of olivine found in diamond-bearing garnet peridotites in Finsch, South Africa and implications for seismic anisotropy. J. Struct. Geol. 70, 12-22. https://doi.org/10.1016/j.jsg.2014.10.015

Li, W., Chen, Y., Yuan, X., Schurr, B., Mechie, J., Oimahmadov, I., Fu, B., 2018. Continental lithospheric subduction and intermediate-depth seismicity: Constraints from S-wave velocity structures in the Pamir and Hindu Kush. Earth Planet. Sci. Lett. 482, 478–489. https://doi.org/10.1016/j.epsl.2017.11.031

Liao, J., Gerya, T., Thielmann, M., Webb, A., Kufner, S.K., Yin, A., 2017. 3D geodynamic models for the development of opposing continental subduction zones: The Hindu Kush-Pamir example. Earth Planet. Sci. Lett. 480, 133-146. https://doi.org/10.1016/j.epsl.2017.10.005

Lin, S.-C., Kuo, B.-Y., 2016. Dynamics of the opposite-verging subduction zones in the Taiwan region: Insights from numerical models. J. Geophys. Res., Solid Earth 121, 2174–2192. https://doi.org/10.1002/2015JB012784

Long, M. D., 2013. Constraints on subduction geodynamics from seismic anisotropy. Rev. Geophys. 51, 76-112. https://doi.org/10.1002/rog.20008

Lynner, C., Long, M.D., 2013. Sub-slab seismic anisotropy and mantle flow beneath the Caribbean and Scotia subduction zones: Effects of slab morphology and kinematics. Earth Plant. Sci. Lett., 361, 367-378. https://doi.org/10.1016/j.epsl.2012.11.007

Lynner, C., Long, M.D., 2014. Sub-slab anisotropy beneath the Sumatra and circum-Pacific subduction zones from source-side shear wave splitting observations. Geochem. Geophys. Geosyst. 15, 2262–2281. https://doi.org/10.1002/2014GC005239

Lynner, C., Long, M.D., Thissen, C.J., Paczkowski, K., Montesi, L.G.J., 2017. Evaluating geodynamic models for sub-slab anisotropy: Effects of olivine fabric type. Geosphere. 13,247-259. https://doi.org/10.1130/GES01395.1

MacDougall, J. G., Jadamec, M. A., Fischer, K. M., 2017. The zone of influence of the subducting slab in the asthenospheric mantle. J. Geophys. Res., Solid Earth 122, 6599–6624. https://doi.org/10.1002/2017JB014445

Mainprice, D., 2007. Seismic anisotropy of the deep earth from a mineral and rock physics perspective. In Treatise on Geophysics, 2, 437-491.

Mohiuddin, A., Long, M.D., Lynner, C., 2015. Mid-mantle seismic anisotropy beneath southwestern Pacific subduction systems and implications for mid-mantle deformation. Phys. Earth Planet. Inter. 245, 1–14.

Nábelek, J., Hetényi, G., Vergne, J., Sapkota, S., Kafle, B., Jiang, M., Su, H.,Chen, J., Huang, B.-S., 2009. Underplating in the Himalaya-Tibet collision zone revealed by the Hi-CLIMB experiment. Science, 325, 1371–1374. doi:10.1126/science.1167719

Negredo, A. M., Replumaz, A., Willaseñor, A., Guillot, S., 2007. Modeling the evolution of continental subduction processes in the Pamir-Hindu Kush region. Earth and Planet. Sci. Lett. 259, 202-225. Doi:10.1016/j.epsl.2007.04.043

Nowacki, A., Kendall, J.-M., Wookey, J., Pemberton, A., 2015. Mid-mantle anisotropy in subduction zones and deep water transport. Geochem. Geophys. Geosyst. 16(3), 764–784. doi:10.1002/2014GC005667

Ohuchi, T., Irifune, T., 2014. Crystallographic preferred orientation of olivine in the Earth's deep upper mantle. Phy. Earth Planet. Inter. 228, 220-231. http://dx.doi.org/10.1016/j.pepi.2013.11.013

Ohuchi, T., Kawazoe, T., Nishihara, Y., Nishiyama, N., Irifune, T., 2011. High pressure and temperature fabric transitions in olivine and variations in upper mantle seismic anisotropy. Earth Planet. Sci. Lett. 304, 55-63, doi:10.1016/j.epsl.2011.01.015

Pavlis, G. L., Das, S., 2000. The Pamir-Hindu Kush seismic zone as a strain marker for flow in the upper mantle. Tectonics 19(1), 103–115. https://doi.org/10.1029/1999tc900062

Replumaz, A., Tapponnier, P., 2003. Reconstruction of the deformed collision zone between India and Asia by backward motion of lithospheric blocks. J. Geophys. Res. 108(B6), 2285, doi:10.1029/2001JB000661.

Russo, R.M., Silver, P.G., 1994. Trench-Parallel Flow Beneath the Nazca Plate from Seismic Anisotropy. Science 263(5150), 1105-1111. DOI: 10.1126/science.263.5150.1105

Russo, R.M., Mocanu, V.I., 2009. Source-side shear wave splitting and upper mantle flow in the Romanian Carpathians and surroundings. Earth Planet. Sci. Lett. 287, 205-216. https://doi.org/10.1016/j.epsl.2009.08.028

Schneider, F., Yuan, X., Schurr, B., Mechie, J., Sippl, C., Haberland, C., et al., GIPP, 2013. Seismic imaging of subducting continental lower crust beneath the Pamir. Earth Planet. Sci. Lett. 375(1), 101–112. https://doi.org/10.1016/j.epsl.2013.05.015

Schoenecker, S.C., Russo, R.M., Silver, P.G., 1997. Source-side splitting of S waves from Hindu Kush-Pamir earthquakes. Tectonophysics 279, 149–159. https://doi.org/10.1016/S0040-1951(97)00130-3

Schulte-Pelkum, V., Monsalve, G., Sheehan, A., Pandey, M. R., Saptota, S., Bilham, R., and Wu, F., 2005. Imaging the Indian subcontinent beneath the Himalaya. Nature 435, 1222-1225, doi:10.1038/nature03678.

Sieminski, A., Liu, Q., Trampert, J., Tromp, J., 2007. Finite-frequency sensitivity of body waves to anisotropy based upon adjoint methods, Geophys. J. Int., 171, 368–389. https://doi.org/10.1111/j.1365-246X.2007.03528.x

Silver, P. G., 1996. Seismic anisotropy beneath the continents: Probing the depths of geology. Annu. Rev. Earth Planet. Sci. 24(1), 385–432. https://doi.org/10.1146/annurev.earth.24.1.385

Sippl, C., Schurr, B., Yuan, X., Mechie, J., Schneider, F. M., Gadoev, M., et al., 2013. Geometry of the Pamir-Hindu Kush intermediate-depth earthquake zone from local seismic data. J. Geophys. Res., Solid Earth 118(4), 1438–1457. https://doi.org/10.1002/jgrb.50128

Sobel, E., Chen, J., Schoenbohm, L., Thiede, R., Stockli, D., Sudo, M., Strecker, M., 2013. Oceanic-style subduction controls late Cenozoic deformation of the Northern Pamir orogeny. Earth Planet. Sci. Lett. 363, 204–218. doi:10.1016/j.epsl.2012.12.009

Song, T.-R. A., Kawakatsu, H., 2012. Subduction of oceanic asthenosphere: evidence from sub-slab seismic anisotropy. Geophys. Res. Lett., 39, L17301. https://doi.org/10.1029/2012GL052639

Song, T.-R. A., Kawakatsu, H., 2013. Subduction of oceanic asthenosphere: a critical appraisal in central Alaska. Earth Planet. Sci. Lett. 367, 82-94. https://doi.org/10.1016/j.epsl.2013.02.010

van der Voo, R., Spakman, W., Bijwaard, H., 1999. Mesozoic subducted slabs under Siberia. Nature 397, 246–249. https://doi.org/10.1038/16686

Walpole, J., Wookey, J., Kendall, J.-M., Masters, T.-G., 2017. Seismic anisotropy and mantle flow below subducting slabs. Earth Plant. Sci. Lett., 465, 155-167. https://doi.org/10.1016/j.epsl.2017.02.023

Wüstefeld, A., Bokelmann, G., 2007. Null detection in shear wave splitting measurements. Bull. Seismol. Soc. Am. 97, 1204–1211. https://doi.org/10.1785/0120060190

Zhang, J. S., Bass, J.D., Schmandt, B., 2018. The Elastic Anisotropy Change Near the 410-km Discontinuity: Predictions From Single-Crystal Elasticity Measurements of Olivine and Wadsleyite. J. Geophys. Res., Solid Earth 123, 2674-2684.https://doi.org/10.1002/2017JB015339

Table 1. Shear moduli, azimuthal anisotropy (A_a), and radial anisotropy (R_a) of olivine provided from literature in deformation coordinates (top half) and mineralogy coordinates (bottom half).

Ref	C44	C55[1]	C66[1]	A_a	R_a	Note
SK12	63.33	65.95	68.64	2.0%	3.0%	Deformation coordinates: 1: lineation (shear direction) 2: perpendicular to 1 in foliation plane 3: normal to foliation (shear plane)
Z18[2]	59.94	71.16	71.74	8.6%	4.7%	
J06C[3]	67.9	71.1	66.6	2.3%	-2.1%	
J06E[3]	65.0	71.1	68.5	4.5%	0.4%	
Z18B	71.16	59.94	71.74	8.6%	4.7%	
J06B[3]	68.9	67.4	69.4	1.1%	0.1%	
LJ15	73.26	67.26	86.45	4.3%	11.0%	
O11[3]	72.50	71.80	74.30	0.5%	1.5%	
SK12	63.33	68.64	65.95	-	-	Mineralogy coordinates: 1: a-axis 2: b-axis 3: c-axis
Z18	59.94	71.74	71.16	-	-	
Z18B	59.94	71.74	71.16			
LJ15	67.26	86.45	73.26	-	-	

Ref: SK12: Song and Kawakatsu (2012); Z18: Zhang et al. (2018); J06B, J06C, and J06E: Jung et al. (2006) for B-type, C-type and E-type olivine, respectively; Z18B: the same as Z18 but assumed to deform as B-type; LJ15: Lee and Jung (2015); O11: Ohuchi et al. (2011). SK12 and Z18 are assumed to deform as A-type. Z18B, LJ15, and O11 deform as B-type.

1. The difference between deformation and mineralogy coordinates is the switches between the 3 shear moduli. Take A-type for instance, the switch is between C55 and C66.

2. Shear moduli calculated for 4 GPa and 1273 K, the same condition as in LJ2015.

3. The elastic moduli measured from deformation experiment is referenced to the deformation geometry. For O11, J06C, J06E, and J06B, the concentrations of crystal exes with respective to lineation and foliation are weak and diffuse, and it is not appropriate to convert them to the intrinsic, mineralogy coordinates.

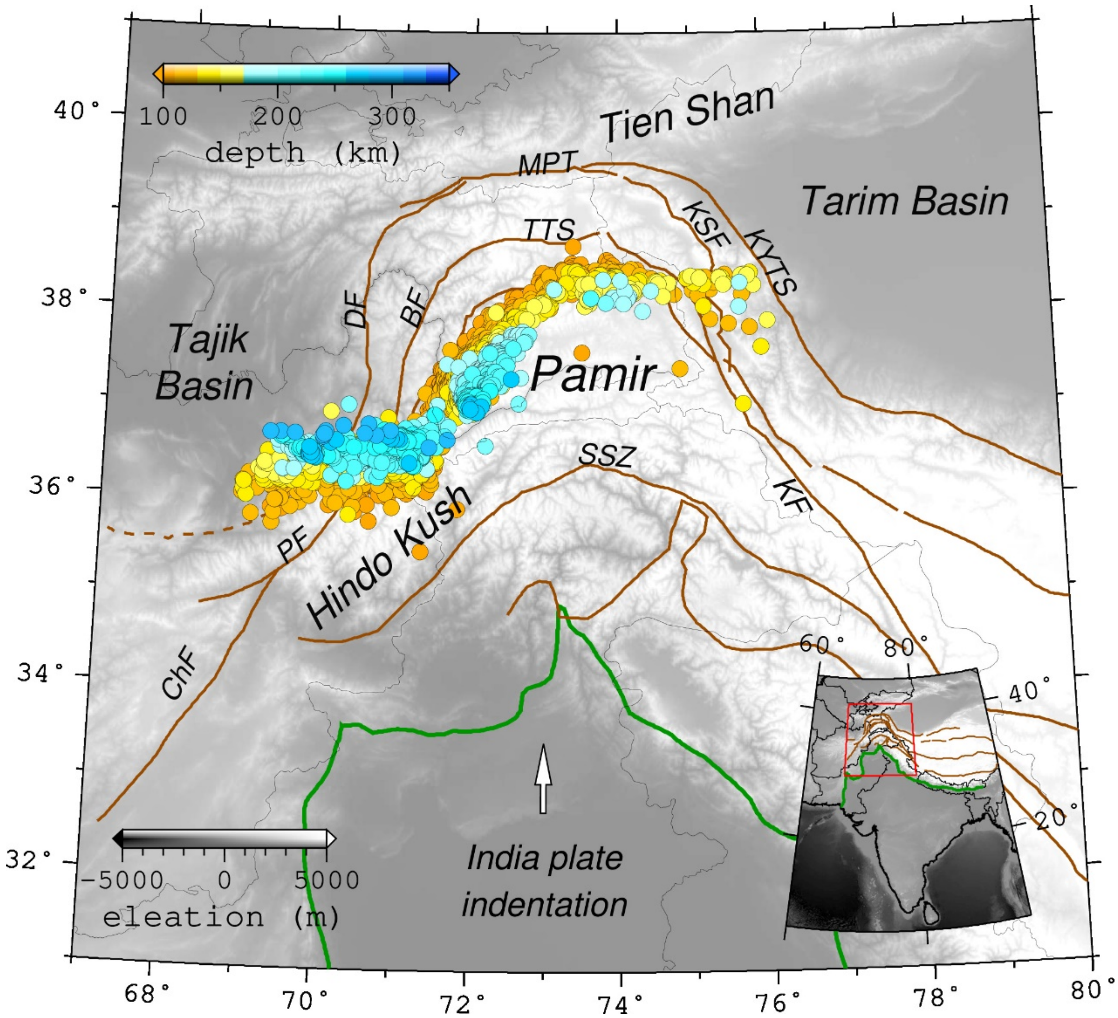

Fig. 1. Map of the Hindu Kush-Pamir region. Earthquakes deeper than 100 km depth depict the geometry of the Hindu Kush slab and the Pamir slab (Kufner et al., 2017). Green line denotes the Eurasian-Asian main thrust boundary and brown lines represent the faults and sutures, adopted from Sippl et al. (2013). ChF: Chaman Fault; PF: Panjshir Fault; DF: Darvaz Fault; BF: Badakhshan Fault; MPT: Main Pamir Fault; TTS: Tanymas Thrust System; KSF: Kongur Shan Fault; KYTS: Kashgar-Yecheng Transfer system; KF: Karakorum Fault; and SSZ: Shyok Suture Zone. The Hindu Kush-Pamir region is outlined in the map on the lower right.

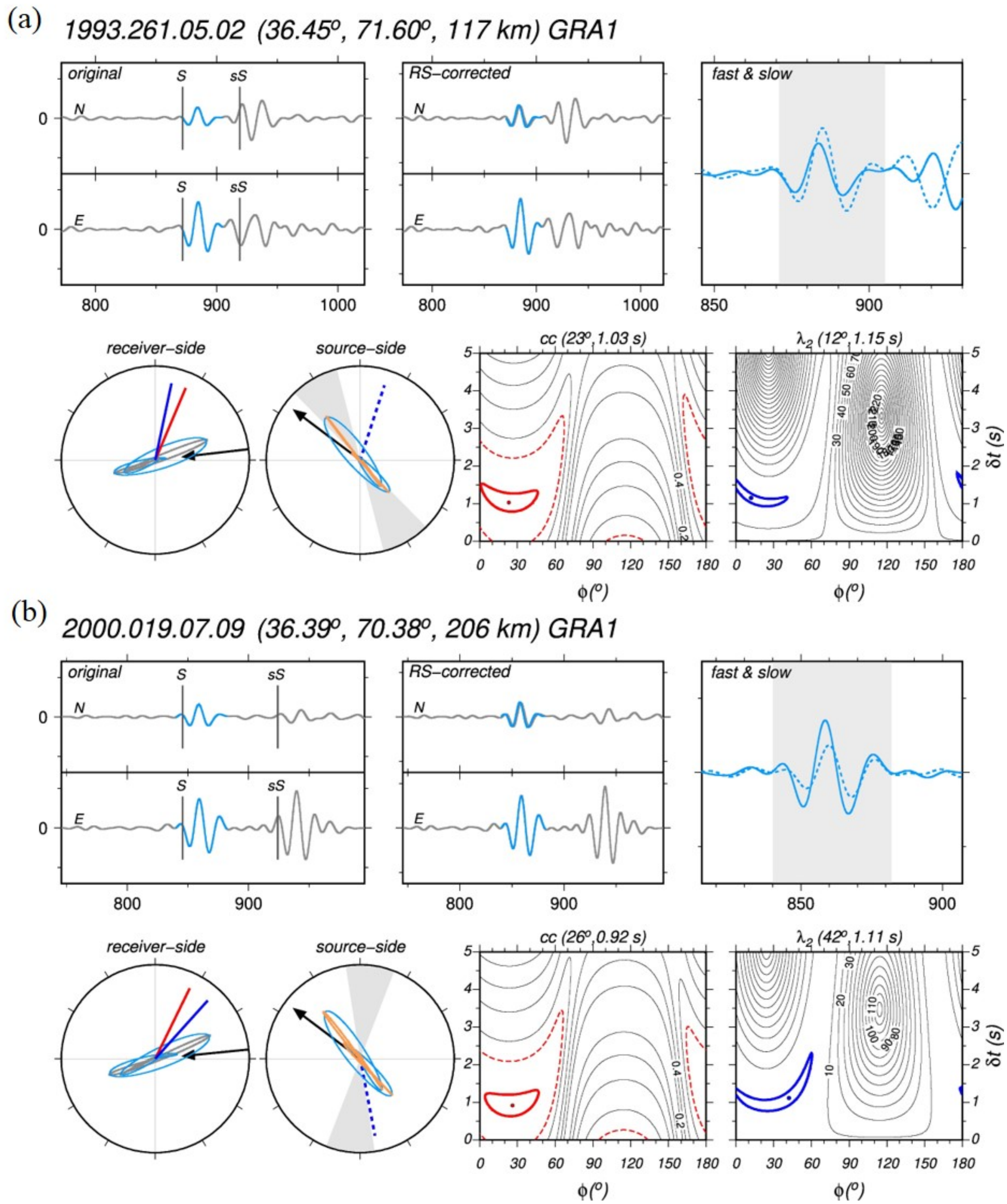
(a)
1993.261.05.02 (36.45°, 71.60°, 117 km) GRA1
original
RS−corrected
fast & slow
S
sS
N
E
receiver−side
source−side
cc (23°,1.03 s)
λ2 (12°,1.15 s)
φ(°)
δt (s)
(b)
2000.019.07.09 (36.39°, 70.38°, 206 km) GRA1
original
RS−corrected
fast & slow
receiver−side
source−side
cc (26°,0.92 s)
λ2 (42°,1.11 s)
φ(°)
δt (s)

Fig. 2. Examples of source-side anisotropy measurement conducted in this study. The one-line label on top of each figure shows date-time of the event (year, Julian day, hour, and minute), location and depth of the event in the parenthesis, and the station name. On the top row, left panel: Original waveforms in NS and EW components with S-wave in measurement window highlighted in blue and the PREM predicted phase arrivals. Middle: Waveforms corrected for receiver-side anisotropy. Right: Waveforms rotated to the fast (solid) and slow (dotted) directions of the source-side anisotropy, with the measurement window in gray. On the lower row, left panel: Information in station frame; S particle motion in gray for the original and light blue for that after receiver-side anisotropy is removed. Two thick lines represent measured fast directions (red for rotation correlation; blue for minimum eigenvalue method). Black arrow indicates where the S wave comes from (at backazimuth). Second panel: Information in the source frame; Curve in light blue is the same in the left panel but translated from the station frame to the source frame; curve in orange is the recovered particle motion after source-side anisotropy is removed. Black arrow indicates the azimuth of S wave. Blue dashed line denotes the ϕ determined from the minimum eigenvalue method. The shaded region represents $\pm 15^{o}$ of the CMT predicted polarization orientation. The CMT solution diagram is shown in Fig. S1. The third and forth panels: Grid search diagrams for rotation correlation method (third; in red) and the minimum eigenvalue method (forth; in blue), respectively, with the best solution denoted by dot, encircled by the contours of the 95% confidence region (sold-line in respective colors) and the contours corresponding to the cross-correlation coefficient of 0.9 (dotted line). (a) Solution accepted. (b) Solution rejected because the recovered particle motion (orange curve) is outside of the CMT prediction region (shade).

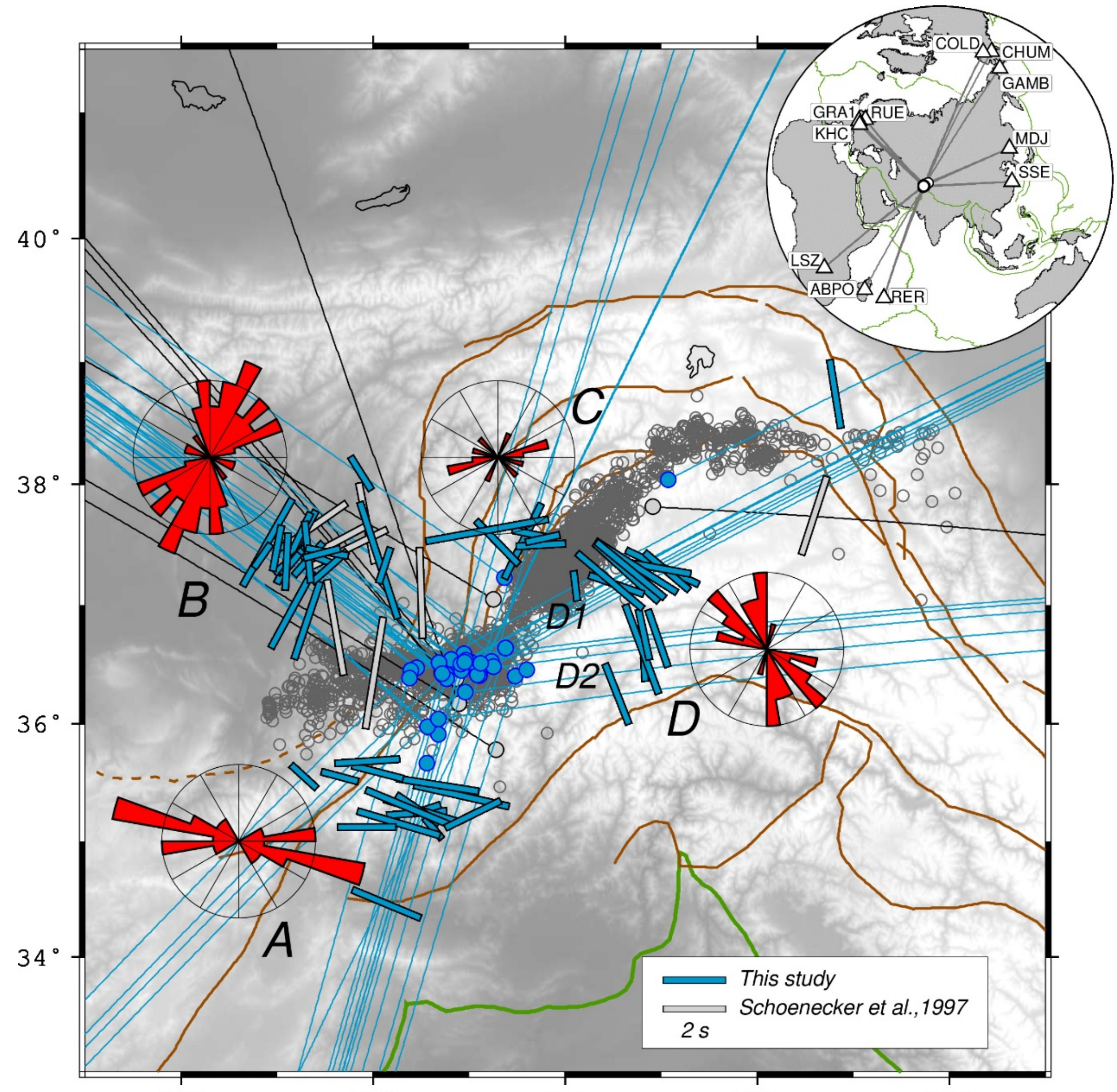

Fig. 3. Source-side anisotropy measurement results. Individual splitting parameters (blue bars) are plotted at locations 200 km down dip along the S raypath from the respective earthquakes (blue dots). The orientation and length of each bar indicate measured ϕ and δt with the 2 s scale in the legend box. Gray bars are the data from Schoenecker et al. (1997). Rose diagram for ϕ is constructed with a 10^{o} bin and an outer rim of 3. The upper right inset shows the stations (triangle) distribution. Group C is disregarded (see Section 3) for having too few measurements. Groups A, B, and D form a circular pattern around the Hindu Kush subduction zone.

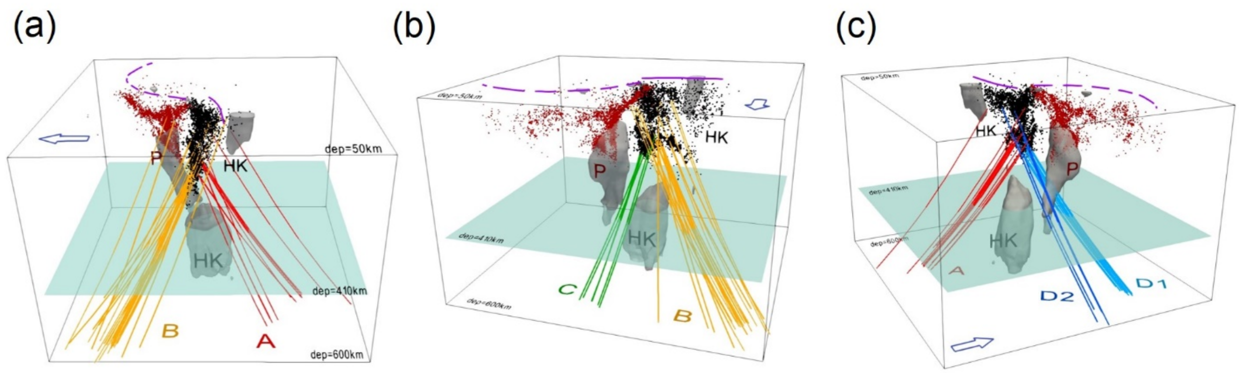

Fig. 4. 3D view of the ray path in three different perspectives. Arrow in each panel points to the north. Top and bottom surfaces of the box are at depths of 50 km and 600 km, respectively. A reference plane is placed at 410 km depth. On the top surface, solid and dashed lines in purple represent convergence boundary for Hindu Kush and Pamir subduction zones, respectively. Black and brown dots represent seismicity in the Hindu Kush and the Pamir slab, respectively. The 2.5% iso-surface of the positive anomalies from Kufner et al. (2016) is plotted to represent the core of the slabs, labeled with HK and P (Pamir). Rays in groups A, B, C, and D are marked in red, orange, green, and blue, respectively. (a) View from the west towards east to show sampling of the south (group A) and north (group B) sides of the HK slab. (b) View from nearly north to show groups B and C north of the HK. (c) View from ESE showing the paths of D1 and D2.

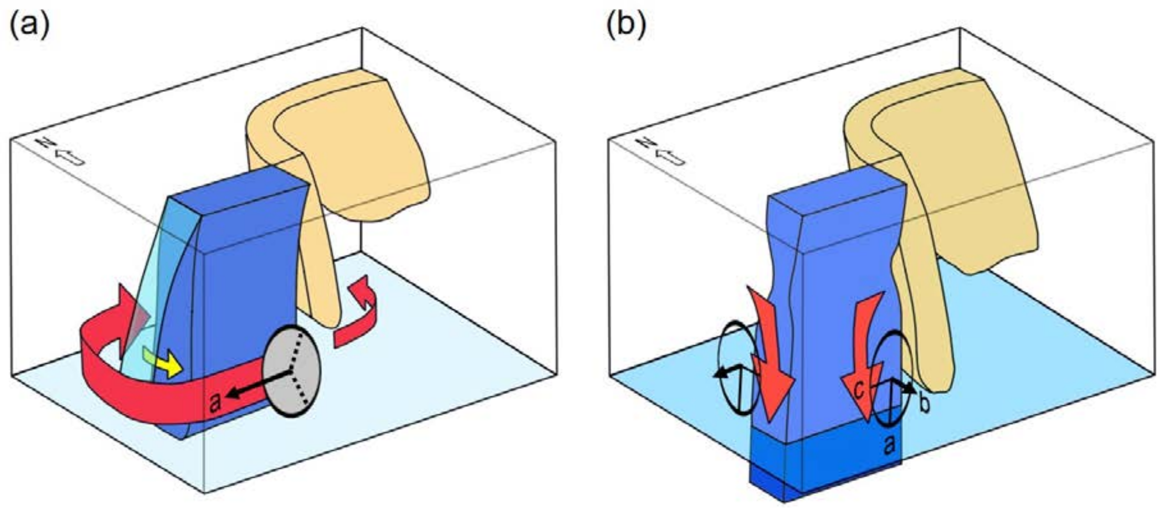

Fig. 5. Cartoons illustrating two mechanisms that are potentially responsible for the observed anisotropy around the HK of the HK (blue) - Parmir (Yellow) double subductions. The top and bottom surfaces of the box correspond to 100 and 410 km depths, respectively. (a) Rollback of the HK slab from a hypothetical north dipping position (transparent light blue) to the current near vertical position (blue), in the pre-breakoff time when the slab extends to 380 km depth (Kufner et al., 2016). Red arrows indicate toroidal flow induced by the rollback. The olivine a-axis is aligned by the pure shear along the toroidal flow, with b- and c-axis within the symmetry plane (shaded). (b) Vertical subduction and the incipient breakoff of the HK lower slab drives downward flow (red arrows) and vertical simple shear. For strong orthorhombic anisotropy, olivine fast plane (a-c plane) is aligned by vertical shear flow and the slow axis (b-axis) is perpendicular to the shear plane.

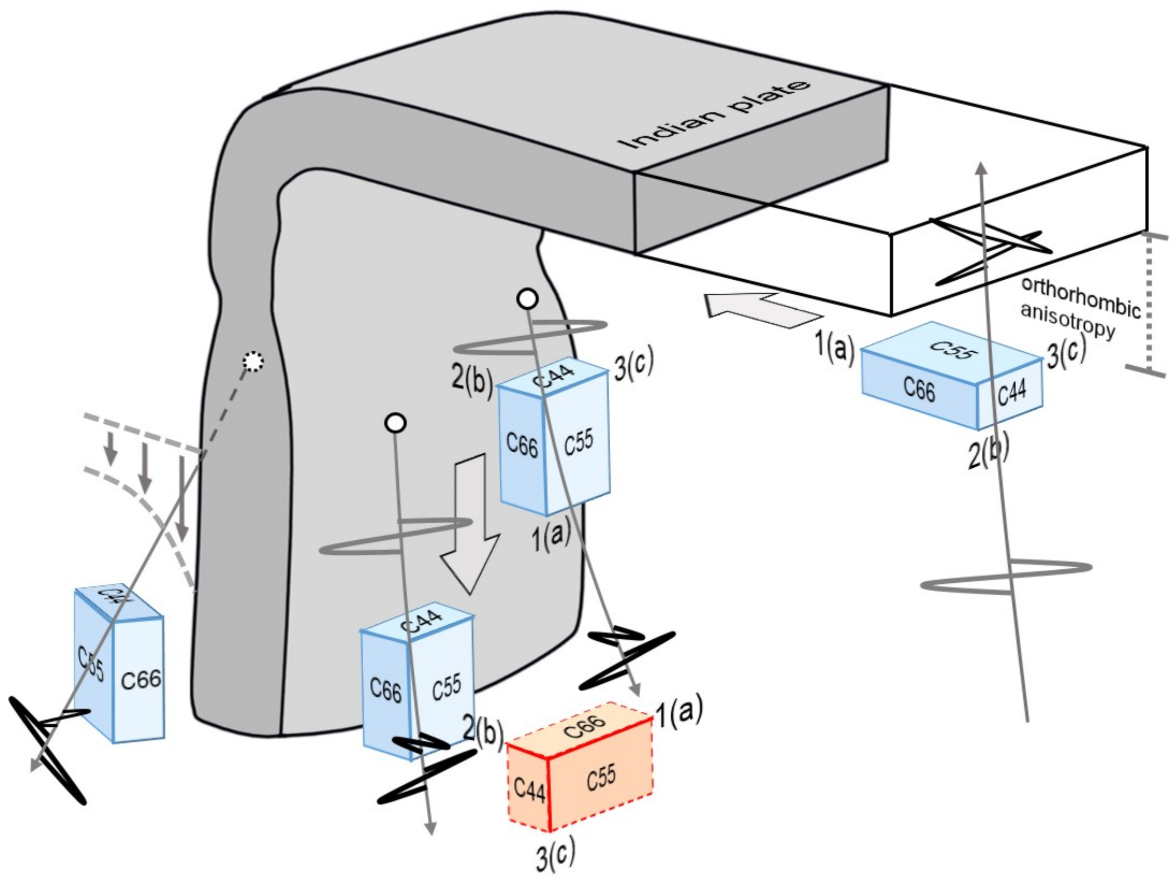

Fig. 6. Schematic illustration of olivine LPO rotation from horizontal to vertical during the Indian plate (gray) subduction in the HK region. Each rectangular box represents olivine fabric with shear modulus labelled on the 3 orthogonal faces in mineralogy convention. In a horizontal flow (horizontal arrow) regime, the alignment of A-type olivine is typified by the box in the upper right corner beneath the Indian plate: Index 1 corresponds to a-axis, index 2 b-axis, and index 3 c-axis. When the A-type fabric is rotated to vertical, S waves traveling sub-vertically from intraslab events (circle) split into fast and slow phases in parallel and perpendicular to slab surface, respectively, if strong orthorhombic anisotropy is present, i.e., C55 > C66 > C44. B-type olivine (orange box) is speculated to form in mid- to lower upper mantle to enhance trench-parallel anisotropy with C55 always significantly larger than C44.

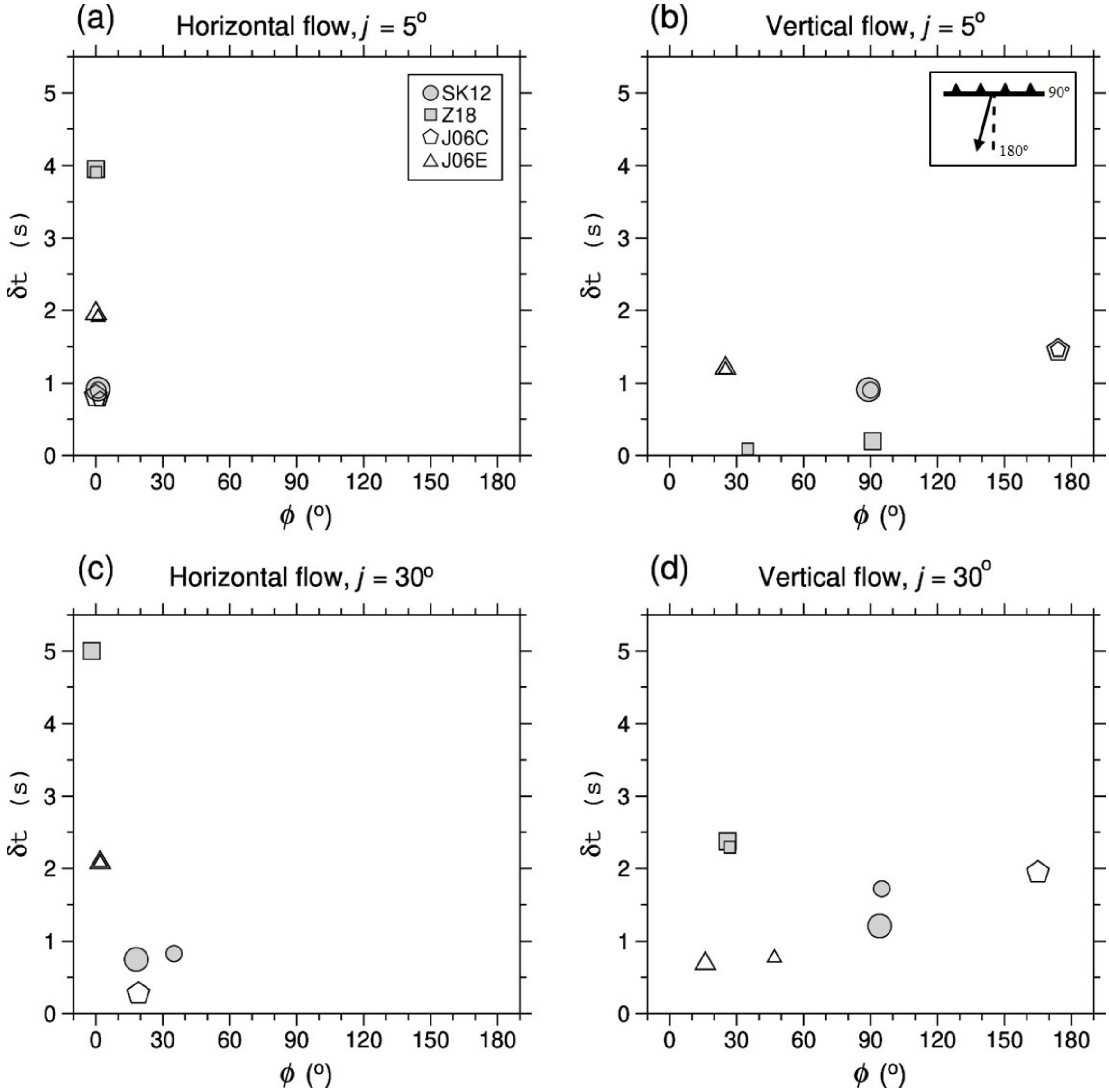

Fig. 7. SWS measurement results of synthetic experiments using elasticity models listed in Table 1 (Shaded symbols for A-type; open symbols for C- and E-type). Panels (a) and (b) with S-wave incidence angle $j = 5^{o}$ provide a reference for an intuitive understanding of the splitting pattern. Panels (c) and (d) represent $j = 30^{o}$. Symbol legend is shown in panel (a), and modeling setting relative to the trench is shown in the inset in panel (b). Trench-normal direction corresponds to the

azimuth of 0 or 180^o and trench-parallel (or slab-parallel) to 90^o. Data shown are only the splitting parameters for S wave at azimuth of 200^o (the arrow in the inset in b) in order to simulate group A. For each model, large-sized symbol denotes an initial polarization in parallel to the azimuth (SV), and small-sized symbol denotes an initial polarization 35^o from SV (SV:SH~0.82:0.57). A-type olivine displays expected trench-normal ϕ for horizontal flow (a), and trench-parallel ϕ for vertical flow (b), except for Z18 for which splitting is small and sensitive to initial polarization. Splitting for C- and E-type olivine mimics that for A-type in horizontal flow, but becomes oblique or perpendicular to the trench in the vertical flow scenario. Variability increases for j = 30^o (c, d) but general patterns remain.

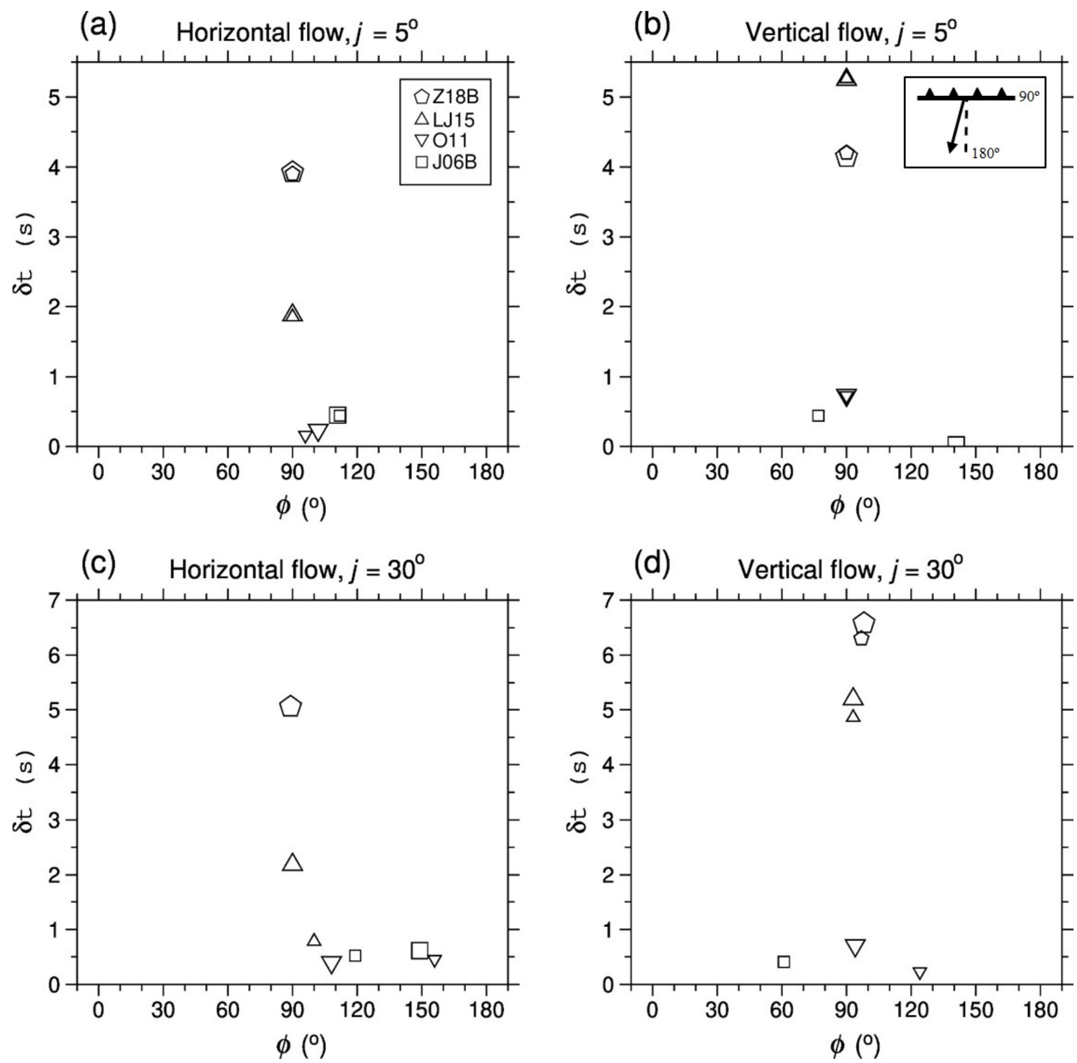

Fig. 8. The same as Figure 7 but for B-type olivine models. Z18B and LJ15 produce mostly trench-parallel ϕ for both horizontal and vertical flow with different incidence angles. For O11 and J06B whose anisotropy is weak, splitting can be polarization sensitive or unresolvable. B-type olivine with trench-parallel splitting is a viable contributor to the observed anisotropy.